Conductance-Matrix Symmetries of a Three-Terminal Hybrid Device

G. C. Ménard,[1,2] G. L. R. Anselmetti,[1,2] E. A. Martinez,[1,2] D. Puglia,[1,2] F. K. Malinowski,[1,2] J. S. Lee,[3] S. Choi,[4] M. Pendharkar,[4] C. J. Palmstrøm,[3,4,5] K. Flensberg,[1] C. M. Marcus,[1,2] L. Casparis,[1,2,*] and A. P. Higginbotham[1,2,†]

[1]*Center for Quantum Devices, Niels Bohr Institute, University of Copenhagen, Universitetsparken 5, 2100 Copenhagen, Denmark*

[2]*Microsoft Quantum–Copenhagen, University of Copenhagen, Universitetsparken 5, 2100 Copenhagen, Denmark*

[3]*California NanoSystems Institute, University of California, Santa Barbara, California 93106, USA*

[4]*Department of Electrical Engineering, University of California, Santa Barbara, California 93106, USA*

[5]*Materials Department, University of California, Santa Barbara, California 93106, USA*

(Received 2 May 2019; published 22 January 2020; corrected 28 January 2020)

We present conductance-matrix measurements of a three-terminal superconductor-semiconductor hybrid device consisting of two normal leads and one superconducting lead. Using a symmetry decomposition of the conductance, we find that antisymmetric components of pairs of local and nonlocal conductances qualitatively match at energies below the superconducting gap, and we compare this finding with symmetry relations based on a noninteracting scattering matrix approach. Further, the local charge character of Andreev bound states is extracted from the symmetry-decomposed conductance data and is found to be similar at both ends of the device and tunable with gate voltage. Finally, we measure the conductance matrix as a function of magnetic field and identify correlated splittings in low-energy features, demonstrating how conductance-matrix measurements can complement traditional single-probe measurements in the search for Majorana zero modes.

DOI: 10.1103/PhysRevLett.124.036802

Symmetry relations for quantum transport are often connected to deep physical principles and make strong predictions for comparison with experiment. For instance, the Onsager-Casimir relations [1–3] arise from microscopic reversibility and were central in early studies of quantum-coherent transport [4–6]. Later, predicted departures from these relations due to interaction effects [7–9], which include bias dependence of the effective potentials, were observed in nonlinear transport [10,11]. The introduction of superconducting terminals results in additional symmetries, as conductance occurs via Andreev reflection from electrons to holes, and is invariant under particle-hole conjugation [12]. For a two-terminal normal-superconducting device, the conductance $g(V)$ is a symmetric function of bias voltage V neglecting interaction effects. As shown in a partner theoretical Letter, for multiterminal superconducting devices $g(V)$ need not be symmetric, although a curious relation exists between the antisymmetric components of the local and nonlocal conductances [13]. These predictions have, to our knowledge, not been tested.

Hybrid superconductor-semiconductor nanowire structures have recently become a topic of intense interest [14–19], motivated in part by proposals for achieving topological superconductivity and Majorana zero modes (MZMs) [20,21]. In two-terminal superconductor-semiconductor devices, observed asymmetries in the subgap conductance [22] have been suggested to arise from a dissipative fermionic reservoir, effectively acting as a third lead [23], although, as in the normal-conducting case [3], bias dependence of the self-consistent potential can also cause a deviation from symmetry [24]. Multiterminal superconducting devices are a topic of particular interest, as they can be used for MZM [25–31], Cooper-pair splitter [32,33], and multiterminal Josephson studies [34–38]. In multiterminal superconducting quantum dot devices, bias asymmetries have been observed [39] and a relationship between nonlocal conductance and the bound-state charge has been proposed [40,41].

In this Letter, we report a symmetry analysis of the conductance matrix measured in a three-terminal, superconductor-semiconductor hybrid device. The antisymmetric components for pairs of conductance-matrix elements are found to qualitatively match at energies below the superconducting gap, with quantitative departures that scale with bias voltage and increase in isolated gate-voltage regions. We use the symmetry-decomposed nonlocal conductance to extract the local charge character of states within the superconducting gap as a function of gate voltage, discovering that the charge is approximately equal on both sides of the device. Finally, we measure local and nonlocal conductances at nonzero magnetic field and identify isolated low-energy states with correlated splittings on each end of the wire, using inferred charge as an additional spectroscopic tool for comparison with theory. This work provides new methods for studying the local charge density of subgap bound states and distinguishing

between topological and trivial states. More generally, it provides a better understanding of the role of symmetry in multiterminal superconducting quantum devices.

Selective area growth (SAG) of InAs nanowires [42,43] is performed by chemical beam epitaxy (CBE) on an InP substrate masked with silicon oxide [44]. The nanowire is half covered by an Al film, which was deposited *in situ* after CBE growth, and is selectively etched to form a superconducting lead. The device [Fig. 1(a)] consists of two normal Ti/Au electrodes (yellow), a central semiconducting region proximitized by Al (blue), a global HfOx dielectric layer, and Ti/Au electrostatic gates (red). We emphasize that the superconducting lead is deposited during growth and contacted remote from the delicate superconductor-semiconductor interface, a benefit of the SAG approach.

Conductance is measured by applying a dc bias voltage $V_{\mathrm{bias}} = V_{R(L)}$ and an ac voltage $\delta V_{R(L)}$ at the right (left) terminal with two different ac excitation frequencies $f_R \sim 18$ Hz and $f_L \sim 42$ Hz. The in-phase ac current $\delta I_{R(L)}$ flowing to the right (left) side is measured with the middle superconducting lead grounded. The device is tunnel coupled to the normal leads by adjusting the two tunnel-gate voltages to $V_{\mathrm{gr}} = -0.485$ V and $V_{\mathrm{gl}} = -1.29$ V, such that $g \ll e^2/h$, which also ensures that the applied voltages drop over the tunnel barriers. We have checked for spurious voltage divider effects using a four-probe measurement on a cold-grounded device, and do not find deviations from the data presented here. The plunger gate voltage V_p is used to tune the chemical potential of the semiconductor. All measurements are performed at base temperature of a dilution refrigerator.

The experimental setup allows the measurement of the 2×2 conductance matrix,

$$g = \begin{bmatrix} g_{LL} & g_{LR} \\ g_{RL} & g_{RR} \end{bmatrix} = \begin{bmatrix} \frac{\delta I_L}{\delta V_L} & -\frac{\delta I_L}{\delta V_R} \\ -\frac{\delta I_R}{\delta V_L} & \frac{\delta I_R}{\delta V_R} \end{bmatrix}, \tag{1}$$

where the sign convention is chosen for compatibility with standard two-terminal measurements of g_{LR}.

Figure 1(b) shows g_{LL} as a function of V_L with $V_R = 0$. Several peaks occur symmetrically around zero bias. We assign the two highest energy peaks to coherence peaks, a signature of the Bardeen-Cooper-Schrieffer (BCS) density of states in the proximitized semiconductor with an induced gap $\Delta \sim 250$ μeV, in agreement with previous observation for similar material systems [43,45]. The other peaks are subgap states with energies $E_0 < \Delta$. Both the high-bias conductance ($V_L > \Delta$) as well as the subgap peak heights are asymmetric in bias [Fig. 1(b)]. The nonlocal conductance g_{LR}, measured as a function of V_R with $V_L = 0$ in Fig. 1(c), exhibits features corresponding to the peaks in g_{LL}. The sign of the peak amplitudes in g_{RL}, however, changes with a sign change in bias, indicating a strong odd component. The remaining conductance-matrix elements

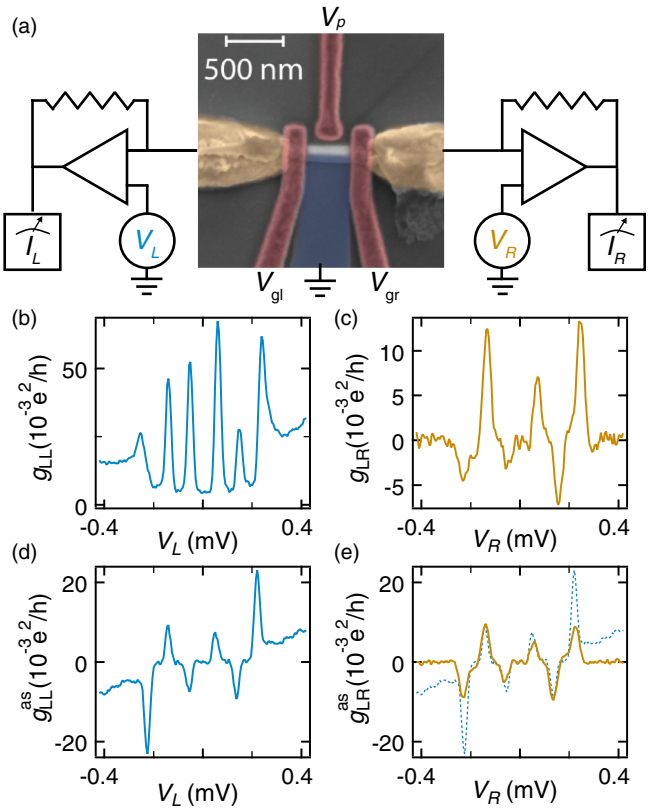

FIG. 1. (a) Colored scanning electron micrograph of the three-terminal device and schematic of the measurement setup. (b) Left side local conductance g_{LL} as a function of left side bias voltage V_L. (c) Left side nonlocal conductance g_{LR} as a function of right side bias voltage V_R. (d) Extracted antisymmetric component of the local conductance g^{as}_{LL} with respect to V_L. (e) Extracted antisymmetric component of the nonlocal conductance g^{as}_{LR} with respect to V_R. The blue dashed line shows g^{as}_{LL} for comparison.

g_{RR} and g_{RL} were also measured and exhibit similar features [46].

To further explore the symmetry properties, the conductance traces are decomposed into their symmetric,

$$g^{\mathrm{s}}(V_{\mathrm{bias}}) = \frac{1}{2}[g(V_{\mathrm{bias}}) + g(-V_{\mathrm{bias}})], \tag{2}$$

and antisymmetric,

$$g^{\mathrm{as}}(V_{\mathrm{bias}}) = \frac{1}{2}[g(V_{\mathrm{bias}}) - g(-V_{\mathrm{bias}})], \tag{3}$$

parts. Figure 1(d) shows g^{as}_{LL} as a function of V_L, which bears a qualitative resemblance to g_{LR}. In fact, g^{as}_{LR}, the antisymmetric component of g_{LR}, closely matches g^{as}_{LL} [dashed line in Fig. 1(e)] for low bias, with some quantitative departures observed at high bias. Reference [13] discusses the identified symmetry relation, $g^{\mathrm{as}}_{LR} = g^{\mathrm{as}}_{LL}$, as an underlying symmetry of the scattering matrix for $V_{\mathrm{bias}} < \Delta$. Departures from this symmetry can result from

bias-voltage dependence of the effective potentials [3], single-particle scattering into the nominally superconducting lead [13], or inelastic processes within the hybrid region [23]. Above the superconducting gap, departures from symmetry scale smoothly with bias voltage, and we have found they persist even when one lead is completely pinched off, which would seem to favor an explanation based on bias-dependent potentials. In addition, we have found that the observed symmetry departures have relatively little field dependence, suggesting that they are not due to the presence of dissipation from vortices.

Next, we investigate the conductance matrix as a function of gate voltage. Figure 2(a) shows g_{LL} (g_{LR}) as a function of V_p and bias V_L (V_R). $g_{LL}(V_p)$ makes the assignment of coherence peaks and subgap states clearer. The coherence peaks do not move when changing the gate voltage, while subgap states appear at different bias voltages for different V_p. We attribute these subgap states to Andreev bound states (ABSs), although it is not entirely clear where the states are confined. We speculate that confinement could result from a Fermi velocity mismatch between the InAs and the Al or disorder in the system. The ABS subgap features are visible as peaks in the nonlocal conductance g_{LR} as well. Pairs of ABS resonances

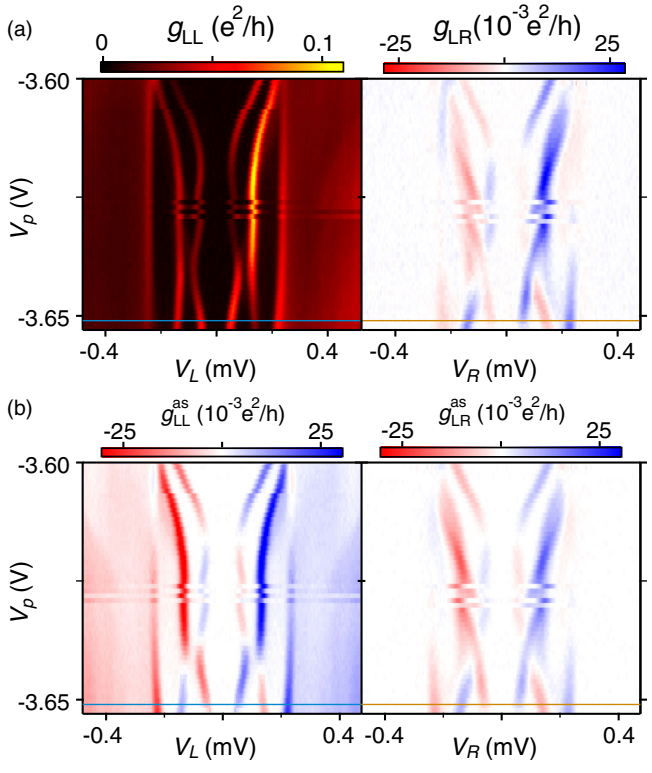

FIG. 2. (a) Local conductance (left-hand panel) and nonlocal conductance (right-hand panel) as a function of plunger gate V_p and bias voltage. (b) Antisymmetric components of local (left) and nonlocal conductance (right) as a function of plunger gate V_p and bias voltage. The colored lines indicate the location of the cuts for the local (blue) and nonlocal (orange) traces in Fig. 1.

at positive and negative bias are found to have opposite sign, again indicating a primarily odd functional form. Symmetry decomposing the datasets as a function of bias yields g^{as}_{LL} and g^{as}_{LR} [Fig. 2(b)], which show a correspondence in general, indicating that the symmetry relationship identified in Fig. 1 is robust as a function of gate voltage. However, in addition to the quantitative high-bias discrepancies already identified in Fig. 1(e), there are isolated regions in Fig. 2(b) where g^{as}_{LL} and g^{as}_{LR} qualitatively differ, associated with crossing of subgap states, e.g., around $V_p \sim -3.64$ V; these regions are presently not understood.

It is interesting to note that ABSs with the same slope with respect to V_p have the same sign in g_{LR}. Further, where the slope changes sign, i.e., at inflection points, the nonlocal conductance disappears and changes sign as well [Fig. 2(a)]. Reference [13] shows that, for a spectrally isolated subgap state at energy E_0, the sign of the nonlocal conductance at bias voltages near $V_0 = E_0/e$ is generally related to the state's local charge density. The symmetric part of the conductance, for a bound state coupled to the left (right) leads at rate $\Gamma_{L(R)}$ and energy $|E_0| > \Gamma_{L(R)}, k_BT$ is

$$g^{s}_{RL}(V_0) = aq_Lq_R, \tag{4}$$

and the antisymmetric part is

$$g^{as}_{RL}(V_0) = an_Lq_R\mathrm{sgn}(V_0), \tag{5}$$

where $q_{L(R)} = u^2_{L(R)} - v^2_{L(R)}$ is the local charge density, $n_{L(R)} = u^2_{L(R)} + v^2_{L(R)}$ is the local probability density, and $u_{L(R)}$, $v_{L(R)}$ are the left (right) Bogoliubov–de Gennes amplitudes. The general expression for a is cumbersome, but in the limiting case $\Gamma_{L(R)} \gg kT$ it takes the simple form, $a = (2e^2/h)[\Gamma_L\Gamma_R/(\Gamma_Ln_L + \Gamma_Rn_R)^2]$. Similar expressions also hold for $g_{LR}(V_0)$. As a consequence, there is a proportionality between the symmetry-decomposed nonlocal conductance and the local charge densities, $g^{s}_{RL}(V_0) \propto q_Lq_R$ and $(g^{as}_{LR})(g^{as}_{RL}) \propto q_Lq_R$.

Proportionality constants can be eliminated by considering the ratio of conductances,

$$Q_L \equiv \frac{g^{s}_{RL}(V_0)}{g^{as}_{RL}(V_0)}\mathrm{sgn}(V_0) \tag{6}$$

$$= \frac{u^2_L - v^2_L}{u^2_L + v^2_L}. \tag{7}$$

Q_L is a measure of the local charge character; $Q_L = +1$ for a state that is locally electronlike ($u \gg v$), and $Q_L = -1$ for a state that is locally holelike ($v \gg u$).

Motivated by these theoretical relations, we compare in Fig. 3(a) the measured symmetric component of a single nonlocal conductance g^{s}_{RL}, with the product of the antisymmetric components of both nonlocal conductances,

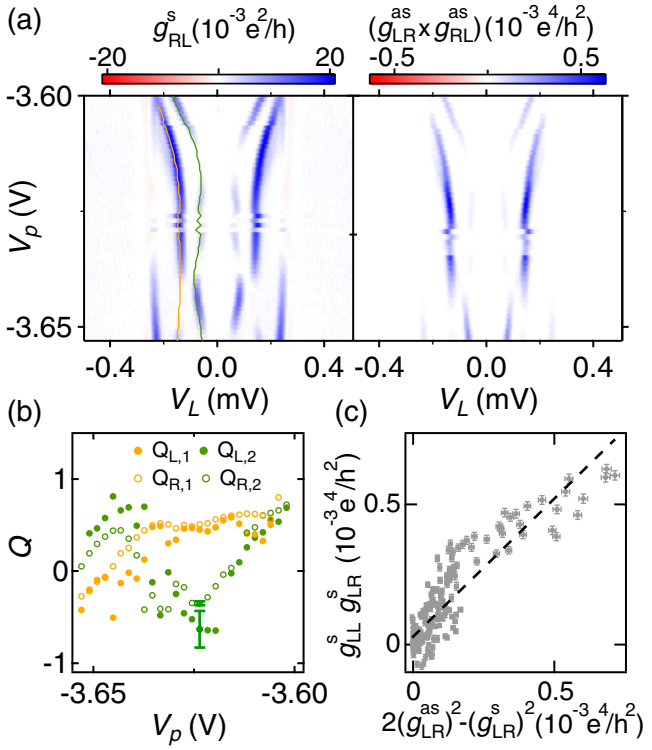

FIG. 3. (a) Symmetric (g^s_{RL}, left-hand panel) and the multiplied antisymmetric ($g^{as}_{LR} \times g^{as}_{RL}$, right-hand panel) components of the nonlocal conductance as a function of plunger gate voltage and bias. The lines indicate the extracted peak positions for the high-energy (orange) and low-energy (green) ABS. (b) Local charge character Q [see Eq. (6)] as a function of V_p for a higher-energy (orange) and lower-energy (green) ABS, for both left (full markers) and right (empty markers) side of the device. The error bars indicate typical errors for extraction of the local charge character [46]. (c) Left side vs right side of Eq. (8) for all identified subgap peaks V_0. Dashed line indicates perfect agreement (slope = 1, intercept = 0).

$(g^{as}_{LR}) \times (g^{as}_{RL})$. The plots in Fig. 3(a) are qualitatively similar, as expected from Eqs. (4) and (5), and suggest that gate dependence of the BCS charge has a dominant effect on the conductance of subgap peaks. To further explore the charge of subgap states, the data are analyzed by extracting peak positions of the ABS resonances from g_{LL}. Decompositions of the nonlocal conductance are evaluated at these positions to obtain $g^s_{RL}(V_0)$ and $g^{as}_{RL}(V_0)$. Q_L is calculated from the peak values for two different subgap states [orange and green lines in Fig. 3(a)]. The local charge character for these states oscillates as a function of V_p, highlighting the gate-tunable charge character of bound state [orange and green markers in Fig. 3(b)]. Sign changes of Q_L indicate that the state is changing from electronlike to holelike, or vice versa. We note that, based on Eq. (6), sign changes g^{as}_{LR} cause sign changes in Q_L. Hence, the correlation between the sign of the nonlocal conductance and dE_0/dV_P is consistent with the charge interpretation. Using g_{LR}, Q_R can be analogously calculated [open markers in Fig. 3(b)], and it is found to be similar to Q_L for both bound states, within experimental error [46]. The similarity between Q_L and Q_R suggests that the particle and hole wave function components, u and v, are rigid on the length scale of the present device, which is unusual for mesoscopic devices where wave functions are often considered to be random and uncorrelated in space.

In theory, when u and v are spatially uniform Ref. [13] predicts that a symmetry relation emerges:

$$g^s_{LL}(V_0)g^s_{LR}(V_0) = 2[g^{as}_{LR}(V_0)]^2 - [g^s_{LR}(V_0)]^2. \quad (8)$$

A parametric plot of the left-hand side vs the right-hand side of Eq. (8) for all identified peaks in the dataset reveals that these quantities are approximately equal [Fig. 3(c)], supporting the view that the coherence factors are spatially uniform. Indeed, performing a linear fit of the data gives a slope of 0.98 ± 0.03 with a small intercept $(0.005)^2 \pm (0.002)^2(e^2/h)^2$, indicating a good general agreement with the relationship predicted by Eq. (8). However, there are regions of gate voltage where systematic deviations from linear behavior are observed, including the previously discussed region $V_P \sim -3.64$ V, where feature crossings are observed in g_{LR}.

Having established the nonlocal conductance as a tool for characterizing subgap states, we now apply a magnetic field while measuring the conductance matrix. Figures 4(a) and 4(d) show the evolution of g_{LL} and g_{RR} in a magnetic field B applied parallel to the wire. The ABSs evolve as a function of B as detected from both ends of the device. As the field initially increases, the low-lying states split. The upper-split states are repelled from higher-lying states, and the lower-split states eventually merge at zero energy. For further increases in field, the low-energy states oscillate around zero energy, a signature typically attributed to hybridized MZM in devices comparable in length to the coherence length [17]. The correlated splitting of zero-bias peaks, measured from both wires ends, was proposed as a "smoking gun" signature of MZM [25], but given the presence of strong correlations at zero magnetic field in this device [31], we suggest that this signature is not by itself conclusive.

The nonlocal conductances g_{LR} and g_{RL} [Figs. 4(b) and 4(c)] as a function of field have asymmetric features corresponding to subgap states in the local conductance, and also exhibit several changes in sign. To study the sign of g_{RL} for the low-energy features, peaks in the local conductance g_{LL} are determined [orange line in Fig. 4(c)], and the peak nonlocal conductance $g_{RL}(V_0)$ is extracted at these points. Of particular interest is the behavior at the field $B^* \sim 0.6$ T, where the energy of the oscillating states has a turning point. The nonlocal conductance at B^* is nonzero [Fig. 4(e)], inconsistent with the expected behavior

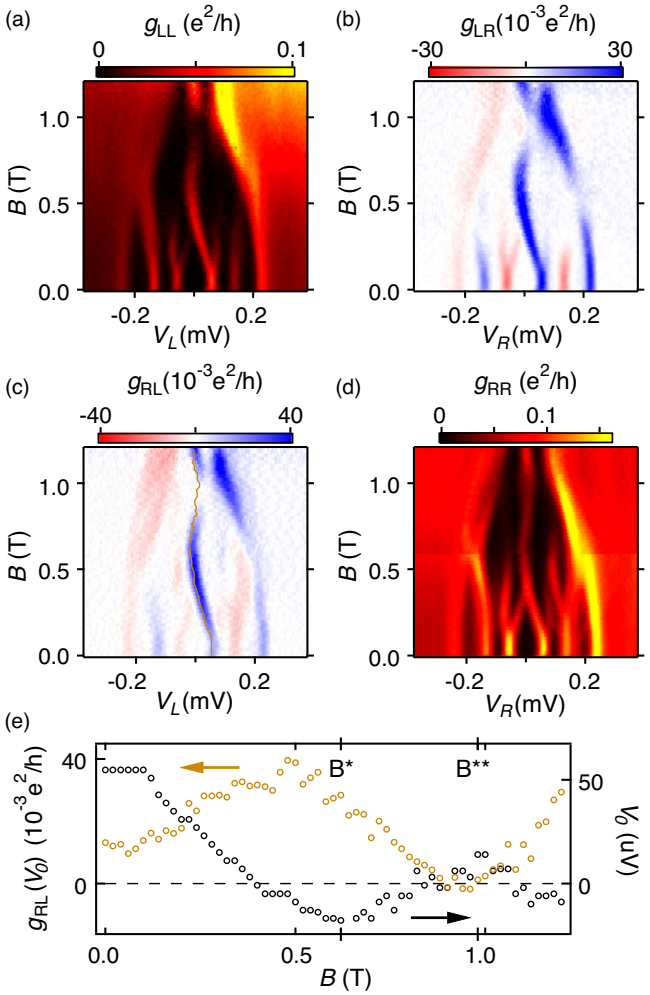

FIG. 4. Local conductances g_{LL} (a) and g_{RR} (d) and nonlocal conductances g_{LR} (b) and g_{RL} (c) as a function of bias voltage and parallel magnetic field B. The orange curve overlayed on (c) indicates peaks found from the local conductance g_{LL}. (e) Peak nonlocal conductance $g_{RL}(V_0)$ (orange) and corresponding bias voltage V_0, (black) as function of magnetic field B. Magnetic fields corresponding to the subgap states' energy-turning points, B^* and B^{**}, are indicated.

for hybridized MZMs, which are chargeless at turning points and therefore have vanishing nonlocal conductance [13,47]. At a higher field $B^{**} \sim 1$ T, there is a second turning point where the nonlocal conductance is small, consistent with the behavior expected for chargeless, hybridized MZMs [48].

Nonlocal transport gives evidence against a Majorana interpretation at intermediate fields ($B < B^{**}$). Intermediate-field effects in hybrid nanowires, in particular the possibility of quasi-Majorana modes that emerge before the true topological transition [29,49–52], have been discussed at length in the literature. It is, to the best of our knowledge, an open theoretical problem to check if quasi-Majorana modes, or other effects [53], can explain the anomalous charge character that we have inferred near B^*. At higher fields ($B > B^{**}$), nonlocal transport does not rule out a topological regime, but an examination of more datasets, and longer device lengths, is required to reach a firm conclusion.

In summary, the observed approximate symmetry relations are consistent with a noninteracting scattering picture and justify the use of symmetry-decomposed conductance to infer the BCS charge. At finite field, we have observed correlated splittings of zero-bias peaks, but find that at intermediate fields their charge character is not consistent with a simple Majorana picture. We anticipate that measurements of the local (on-diagonal) conductance, combined with the insights from the nonlocal (off-diagonal) conductance, will play an important role in substantiating the existence of MZMs.

We acknowledge helpful discussions with Jeroen Danon, Roman Lutchyn, Dima Pikulin, and Torsten Karzig. This work was supported by Microsoft Project Q and the Danish National Research Foundation. C. M. M. acknowledges support from the Villum Foundation.

L. C. and A. P. H. contributed equally to this work.

*lucas.casparis@microsoft.com
†andrew.higginbotham@ist.ac.at

[1] L. Onsager, Phys. Rev. **38**, 2265 (1931).
[2] H. B. G. Casimir, Rev. Mod. Phys. **17**, 343 (1945).
[3] M. Büttiker, IBM J. Res. Dev. **32**, 317 (1988).
[4] R. A. Webb, S. Washburn, C. P. Umbach, and R. B. Laibowitz, Phys. Rev. Lett. **54**, 2696 (1985).
[5] A. D. Benoit, S. Washburn, C. P. Umbach, R. B. Laibowitz, and R. A. Webb, Phys. Rev. Lett. **57**, 1765 (1986).
[6] M. Büttiker, Phys. Rev. Lett. **57**, 1761 (1986).
[7] T. Christen and M. Bttiker, Eur. Phys. Lett. **35**, 523 (1996).
[8] B. Spivak and A. Zyuzin, Phys. Rev. Lett. **93**, 226801 (2004).
[9] D. Sánchez and M. Büttiker, Phys. Rev. Lett. **93**, 106802 (2004).
[10] A. Löfgren, C. A. Marlow, I. Shorubalko, R. P. Taylor, P. Omling, L. Samuelson, and H. Linke, Phys. Rev. Lett. **92**, 046803 (2004).
[11] D. M. Zumbühl, C. M. Marcus, M. P. Hanson, and A. C. Gossard, Phys. Rev. Lett. **96**, 206802 (2006).
[12] A. F. Andreev, Zh. Eksp. Teor. Fiz. **46**, 1823 (1964) [Sov. Phys. JETP **19**, 1228 (1964)].
[13] J. Danon, A. B. Hellenes, E. B. Hansen, L. Casparis, A. P. Higginbotham, and K. Flensberg, preceding Letter, Phys. Rev. Lett. **124**, 036801 (2020).
[14] V. Mourik, K. Zuo, S. M. Frolov, S. R. Plissard, E. P. A. M. Bakkers, and L. P. Kouwenhoven, Science **336**, 1003 (2012).
[15] A. Das, Y. Ronen, Y. Most, Y. Oreg, M. Heiblum, and H. Shtrikman, Nat. Phys. **8**, 887 (2012).
[16] H. O. H. Churchill, V. Fatemi, K. Grove-Rasmussen, M. T. Deng, P. Caroff, H. Q. Xu, and C. M. Marcus, Phys. Rev. B **87**, 241401(R) (2013).

[17] S. M. Albrecht, A. Higginbotham, M. Madsen, F. Kuemmeth, T. S. Jespersen, J. Nygård, P. Krogstrup, and C. M. Marcus, Nature (London) **531**, 206 (2016).
[18] M. T. Deng, S. Vaitiekenas, E. B. Hansen, J. Danon, M. Leijnse, K. Flensberg, J. Nygård, P. Krogstrup, and C. M. Marcus, Science **354**, 1557 (2016).
[19] H. Zhang *et al.*, Nature (London) **556**, 74 (2018).
[20] R. M. Lutchyn, J. D. Sau, and S. Das Sarma, Phys. Rev. Lett. **105**, 077001 (2010).
[21] Y. Oreg, G. Refael, and F. von Oppen, Phys. Rev. Lett. **105**, 177002 (2010).
[22] Ö. Gül, H. Zhang, J. D. S. Bommer, M. W. A. de Moor, D. Car, S. R. Plissard, E. P. A. M. Bakkers, A. Geresdi, K. Watanabe, T. Taniguchi, and L. P. Kouwenhoven, Nat. Nanotechnol. **13**, 192 (2018).
[23] C.-X. Liu, J. D. Sau, and S. Das Sarma, Phys. Rev. B **95**, 054502 (2017).
[24] J. Chen, P. Yu, J. Stenger, M. Hocevar, D. Car, S. R. Plissard, E. P. A. M. Bakkers, T. D. Stanescu, and S. M. Frolov, Sci. Adv. **3**, e1701476 (2017).
[25] S. Das Sarma, J. D. Sau, and T. D. Stanescu, Phys. Rev. B **86**, 220506(R) (2012).
[26] B. M. Fregoso, A. M. Lobos, and S. Das Sarma, Phys. Rev. B **88**, 180507(R) (2013).
[27] T. D. Stanescu and S. Tewari, Phys. Rev. B **89**, 220507(R) (2014).
[28] T. O. Rosdahl, A. Vuik, M. Kjaergaard, and A. R. Akhmerov, Phys. Rev. B **97**, 045421 (2018).
[29] C. Reeg, O. Dmytruk, D. Chevallier, D. Loss, and J. Klinovaja, Phys. Rev. B **98**, 245407 (2018).
[30] Y.-H. Lai, J. D. Sau, and S. Das Sarma, Phys. Rev. B **100**, 045302 (2019).
[31] G. L. R. Anselmetti, E. A. Martinez, G. C. Méenard, D. Puglia, F. K. Malinowski, J. Lee, S. Choi, M. Pendharkar, C. J. Palmstrøm, C. M. Marcus, L. Casparis, and A. P. Higginbotham, Phys. Rev. B **100**, 205412 (2019).
[32] L. Hofstetter, S. Csonka, J. Nygård, and C. Schönenberger, Nature (London) **461**, 960 (2009).
[33] L. G. Herrmann, F. Portier, P. Roche, A. L. Yeyati, T. Kontos, and C. Strunk, Phys. Rev. Lett. **104**, 026801 (2010).
[34] B. van Heck, S. Mi, and A. R. Akhmerov, Phys. Rev. B **90**, 155450 (2014).
[35] E. Strambini, S. D'Ambrosio, F. Vischi, F. S. Bergeret, Y. V. Nazarov, and F. Giazotto, Nat. Nanotechnol. **11**, 1055 (2016).
[36] J. S. Meyer and M. Houzet, Phys. Rev. Lett. **119**, 136807 (2017).
[37] H.-Y. Xie, M. G. Vavilov, and A. Levchenko, Phys. Rev. B **96**, 161406(R) (2017).
[38] N. Pankratova, H. Lee, R. Kuzmin, M. Vavilov, K. Wickramasinghe, W. Mayer, J. Yuan, J. Shabani, and V. E. M. Manucharyan, arXiv:1812.06017.
[39] L. Hofstetter, S. Csonka, A. Baumgartner, G. Fülöp, S. d'Hollosy, J. Nygård, and C. Schönenberger, Phys. Rev. Lett. **107**, 136801 (2011).
[40] J. Schindele, A. Baumgartner, R. Maurand, M. Weiss, and C. Schönenberger, Phys. Rev. B **89**, 045422 (2014).
[41] J. Gramich, A. Baumgartner, and C. Schönenberger, Phys. Rev. B **96**, 195418 (2017).
[42] F. Krizek, J. E. Sestoft, P. Aseev, S. Marti-Sanchez, S. Vaitiekėnas, L. Casparis, S. A. Khan, Y. Liu, T. Stankevič, A. M. Whiticar, A. Fursina, F. Boekhout, R. Koops, E. Uccelli, L. P. Kouwenhoven, C. M. Marcus, J. Arbiol, and P. Krogstrup, Phys. Rev. Mater. **2**, 093401 (2018).
[43] S. Vaitiekėnas, A. M. Whiticar, M.-T. Deng, F. Krizek, J. E. Sestoft, C. J. Palmstrøm, S. Marti-Sanchez, J. Arbiol, P. Krogstrup, L. Casparis, and C. M. Marcus, Phys. Rev. Lett. **121**, 147701 (2018).
[44] J. S. Lee *et al.*, Phys. Rev. Mater. **3**, 084606 (2019).
[45] W. Chang, S. M. Albrecht, T. S. Jespersen, F. Kuemmeth, P. Krogstrup, J. Nygård, and C. M. Marcus, Nat. Nanotechnol. **10**, 232 (2015).
[46] See Supplemental Material at http://link.aps.org/supplemental/10.1103/PhysRevLett.124.036802 for extended dataset, correlation, and error analysis.
[47] E. B. Hansen, J. Danon, and K. Flensberg, Phys. Rev. B **97**, 041411(R) (2018).
[48] At B^{**}, Q has large error bars due to small signal, but from Eqs. (4) and (5), $g_{RL}(\pm V_0) = 0$ implies $q_R = 0$ for nonzero couplings.
[49] J. Cayao, E. Prada, P. San-Jose, and R. Aguado, Phys. Rev. B **91**, 024514 (2015).
[50] C.-X. Liu, J. D. Sau, T. D. Stanescu, and S. Das Sarma, Phys. Rev. B **96**, 075161 (2017).
[51] A. Vuik, B. Nijholt, A. R. Akhmerov, and M. Wimmer, SciPost Phys. **7**, 061 (2019).
[52] F. Peñaranda, R. Aguado, P. San-Jose, and E. Prada, Phys. Rev. B **98**, 235406 (2018).
[53] F. Domínguez, J. Cayao, P. San-Jose, R. Aguado, A. L. Yeyati, and E. Prada, npj Quantum Mater. **2**, 13 (2017).

Correction: The article identification number for this Letter was assigned incorrectly and has been fixed.